Deformation mechanisms of FeCoCrNiMo0.2 high entropy alloy at 77 and 15 K

Tang, Lei; Cai, Biao; Attallah, Moataz

DOI:
10.1016/j.scriptamat.2019.11.026

Document Version
Peer reviewed version

Citation for published version (Harvard):
Tang, L, Cai, B & Attallah, M 2020, 'Deformation mechanisms of FeCoCrNiMo0.2 high entropy alloy at 77 and 15 K', *Scripta Materialia*, vol. 178, pp. 166-170. https://doi.org/10.1016/j.scriptamat.2019.11.026

Deformation mechanisms of $FeCoCrNiMo_{0.2}$ high entropy alloy at 77 and 15 K

Lei Tang[a], Kun Yan[b], Biao Cai[a], Yiqiang Wang[c], Bin Liu[d], Saurabh Kabra[e], Moataz M Attallah[a], Yong Liu[d**]*

a. School of Metallurgy and Materials, University of Birmingham, B15 2TT, UK

b. School of Materials, University of Manchester, M13 9PL, UK

c. United Kingdom Atomic Energy Authority, Culham Science Centre, Abingdon, OX14 3DB, UK

d. State Key Laboratory for Powder Metallurgy, Central South University, 410083, P.R. China

e. ISIS Facility, Rutherford Appleton Laboratory, Didcot, OX11 0QX, UK

** Corresponding author.*

Abstract:

Deformation mechanisms of high entropy alloys (HEAs) at cryogenic temperatures have attracted extensive research interest. We used *in situ* neutron diffraction to study the tensile behavior of a face-centered-cubic HEA at 77 and 15 K and compared its stacking fault energy (SFE) at ambient and cryogenic temperatures. The SFE dropped from 28 mJm^{-2} at 293 K to 11 mJm^{-2} at 15 K, leading to the transition of deformation mechanism from deformation-induced twinning to martensite phase transformation. As a result, excellent balance of strength and ductility was achieved at both temperatures. This finding highlights the importance of SFE for cryogenic alloy design.

Key words: High entropy alloy; Cryogenic deformation; neutron diffraction;

Differing from traditional alloys, which are mainly based on only one principle element, high entropy alloys (HEAs) were designed to consist of near equimolar multi-components and single phase to maximize their configurational entropy [1-4]. The unique features of HEAs (sluggish diffusion, cocktail effects and high lattice distortion [1, 3]) usually come with eminent mechanical performance [5-9]. Researches have shown that at cryogenic temperatures several HEAs (FeCoCrNi [10], CrMnFeCoNi [11], FeCoNiCr [12], et al.) with single face-centered cubic (FCC) phase have an excellent combination of high strength and elongation, making them very attractive for low-temperature applications, such as liquified natural gas industry, structural material for superconductor in fusion reactors and outer space.

Two athermal transformations are known to significantly improve HEAs' mechanical performance: deformation-induced twinning and phase transformation [13]. It is well established that deformation-induced nano-twinning can activate dynamic Hall-Petch effect, leading to significant increments in both strength and ductility [14]. Phase transformation also serves as an important origin of strength and ductility in FCC alloys by inducing (transformation-induced-plasticity) TRIP effect [15]. The dominant factor in deciding the strengthening mechanisms in HEAs is found to be the stacking fault energy (SFE, γ_{sf}) of the alloy [12], which is mainly affected by alloy composition and deformation conditions (e.g. temperature and strain rate). According to previous studies [14, 16, 17], dislocation passage and piling up dominates the plastic deformation when SFE exceeds 45 mJm^{-2}, while twinning will be more favorable with SFE in the range of 15~45 mJm^{-2}. If SFE lowers to less than 15 mJm^{-2}, the phase transformation from FCC-austenite to martensite with hexagonal-close-packed (HCP) and/or body-centered-cubic (BCC) structure can be triggered.

Temperature is one of the dominant factors in deciding alloys' SFE- the lower the temperature, the lower the SFE- hence controlling the micro-mechanical behavior. SFE of FeCoNiCr alloy at room temperature has been determined in the range of 23 to 31 mJ/m^2 by transmission electron microscopy [18], and 17.4 to 31.7 mJ/m^2 by X-ray diffraction and *ab initio* calculation [19]. Twinning and dislocation pilling up are the main deformation mechanism of a HEA from room temperature to 77 K [12]. However, some researches

show that via tuning the alloy composition [20], phase transformation can also be induced during plastic deformation of HEAs at room temperature [8] and 77 K [21]. Mechanical performance and deformation mechanisms of HEAs at extremely low temperatures (≤ 77 K), however, have scarcely been reported. Lin *et al.* recently reported FCC to HCP phase transformation when FeCoCrNi alloy was deformed at 4.5 K [10], in contrast to twinning reported at higher temperatures. Therefore, it is of great interest to perform mechanical testing at temperature below 77 K, and to compare the micro-mechanical behavior of the HEAs at different temperatures.

In this study, we have carried out *in situ* neutron diffraction on a $FeCoCrNiMo_{0.2}$ HEA at 77 and 15 K with the aim to probe its strengthening origins. This study provides a better understanding of the relationship among SFE, temperature and mechanical properties of HEA and sheds a light on designing engineering alloys with better combination of strength and ductility for cryogenic applications.

A HEA ($FeCoCrNiMo_{0.2}$) was prepared by powder metallurgy as detailed in Ref. [22]. The ENGIN-X diffractometer (ISIS spallation neutron source, the Rutherford Appleton Laboratory, UK) was utilized to perform the *in situ* time of flight neutron diffraction during the tensile tests. Dog-bone tensile samples with gauge dimension of Φ 8 × 34.5 mm were machined. The tensile tests were carried out by a 100 kN Instron stress rig with a cryogenic chamber cooled by liquid helium [23]. The loading direction orientated 45° relative to the incident neutron beam. Two detectors (axial and radial) are capable of capturing diffraction signals parallel and perpendicular to the loading direction. The gauge volume for neutron diffraction measurements was 4 × 4 × 4 mm^3 and each diffraction pattern collection consumed 20 mins.

Representative strain-stress curves of the alloy at 293 [22], 77 and 15 K are shown in Fig. 1a. The alloy showed large yielding strength (YS) of 376 MPa, ultimate tensile strength (UTS) of 767 MPa along with excellent total elongation of 52.5% at 293 K at 293 K (Table 1). At 77 K, the YS, UTS and total elongation all enhanced to 637 MPa, 1212 MPa and 71.2%, respectively. At 15 K, the YS further increased to 710 MPa, UTS to 1423 MPa and the ductility dropped slightly to 41.8%. As shown in Fig. 1a, the true stress-strain curves at 293 and 77 K show a very similar pattern, whereas the one at 15 K was different, which consisted of a plateau period within 0.02 to 0.12 true strain followed by an uptrend.

Strain hardening rate (SHR) curves (shown in Fig. 1b) at 293 and 77 K shared a quite similar trend. They both experienced a rapid drop at the initial stage, then the decreasing rates slowed down until fracture. SHR at 77 K exhibited an overall higher value than that at 293 K. In contrast, SHR at 15 K changed more abruptly and showed an unusually large strain-hardening capability. Three pronounced stages can be observed as outlined in Fig. 1b: starting from a very large value of ~7600, the SHR curve initially dropped dramatically to the bottom of ~60, corresponding to the plateau period in stress-strain curve. It then soared to a peak of ~7500 with true stress of ~1270 MPa, characterizing the stage II, after which it began dropping until facture (Stage III).

The diffraction patterns collected at axial direction during tensile loading at 77 and 15 K are plotted in Fig. 2a and 2b, respectively. The sample at room temperature composes of a single FCC phase with lattice parameter of 3.595 Å and no new phases appeared during cooling. The lattice parameter of FCC-phase decreased to 3.586 Å at 77 K and 3.584 Å at 15 K. During tensile testing at 77 K no new phase was observed (Fig. 2a). At 15 K (Fig. 2b), peaks belonging to FCC-phase were replaced progressively by newly formed peaks after yielding, which were identified as HCP/BCC- phases via TOPAS [24]. Fig. 2c shows the diffraction pattern between d spacing=2.125~1.75 Å, clearly demonstrating the occurrence of phase transformation. Formation of HCP/BCC- phases of the FCC HEA during tensile loading is similar to austenite steels and transformation-induced-plasticity steels [25], so we simply use γ, ε and α' to respectively symbolize FCC-, HCP- and BCC- phases.

The change in lattice strain was measured with the following formula [12]:

$$\varepsilon_{hkl} = \frac{d_{hkl} - d^0_{hkl}}{d^0_{hkl}} \quad (1)$$

, where ε_{hkl}, d_{hkl} and d^0_{hkl} correspond to the lattice strain, inter-planar spacing under stress, stress-free lattice spacing of {hkl} crystallographic grain family, respectively. The d spacing was obtained by fitting single reflection with Pseudo-Voigt function using GSAS program [26]. Fig. 3a and 3c show the evolution of elastic lattice strain from axial and radial direction in different grain families during tensile deformation at 77 and

15 K, respectively. It is noted that, the lattice strain at 15 K was depicted only at low strain conditions (≤0.15) because the occurrence of new peaks overlapped with the original peaks, leading to high inaccuracy during single peak fitting of γ-phase peaks at larger strains. A linear relationship was kept before yielding at both temperatures. The slope of the curves at 15 K changed more abruptly than that at 77 K after yielding due to the phase transformation and the following stress partitioning.

Studies have shown that if stacking faults (SFs) formed during deformation, shift of the peak positions for successive orders of reflections such as {111} and {222} will be different due to the structure factor for SFs [27]. We present the lattice strain evolution of two successive grain planes of {111} and {222} at axial and radial directions at both temperatures (only strain $\leqslant 0.15$ is illustrated at 15 K) in Fig. 3b and 3d, respectively. The lattice strain of {111} and {222} reflection deviated from each other after certain stress/strain was reached, confirming the formation of SFs.

The peak shifting can be ascribed to two main sources: macro-strain ($\varepsilon_{hkl}^{strain}$) and SFs ($\varepsilon_{hkl}^{sf}$), following a relationship [28, 29] of:

$$\varepsilon_{hkl}^{exp} = \varepsilon_{hkl}^{strain} - \varepsilon_{hkl}^{sf} = \varepsilon_{hkl}^{strain} - \frac{\sqrt{3}}{4\pi}\frac{\sum b \pm (h+k+l)}{(u+b)(h^2+k^2+l^2)}SFP \quad (2)$$

, where the ε_{hkl}^{exp} is the measured lattice strain, SFP represents stacking fault probability, while *u* and *b* are the numbers of non-broadened and broadened components due to SFs [28]. Accordingly, Fig. 3b and 3d illustrate the SFP change with respect to true strain at 77 and 15 K. After SFP surpassed 0, it increased almost linearly as a function of true strain. The fitted line representing the SFP at 77 K showed a gentle slope of ~55 (Fig. 3b), which boosted to ~319 when the temperature dropped to 15 K (Fig. 3d). SFP increased to 42 $\times 10^{-3}$ at 15 K at only 0.13 true strain, whereas it increased to only 24 $\times 10^{-3}$ at 77 K at 0.52 true strain. This indicated that at 15 K, the alloy has much higher probability to form SFs than at 77 K.

SFE, which indicates the ease of dissociating perfect dislocations into partial dislocations and SFs, can be estimated according to Reed and Schramm [30]:

$$\gamma_{sf} = \frac{6.6a_0}{\pi\sqrt{3}}\left(\frac{2c_{44}}{c_{11}-c_{12}}\right)^{-0.37}\frac{\langle\varepsilon_{50}^2\rangle_{111}}{SFP}\left(\frac{c_{44}+c_{11}-c_{12}}{3}\right) \quad (3)$$

, where $\langle\varepsilon_{50}^2\rangle_{111}$represents mean square strain calculated by deconvoluting size and strain broadening effects with double-Voigt method [31], c_{11}, c_{12} and c_{44} are the elastic constants obtained from single crystals. Based on the *ab initio* simulation from [20], c_{11}=216 GPa, c_{12}=175 GPa and c_{44}=189 GPa were used here. The SFE evolution of the alloy at 293, 77 and 15 K was plotted as a function of true strain in Fig. 4a. All three fitted curves showed a similar trend that they continued to drop at lower strain until reaching the turning points and then kept at constant values, corresponding to the SFE of the alloy (Table 1). At low strain conditions, the calculated high SFE values are artifacts of Eq. 3 due to the fact that the formed SFs are not enough to be reflected in diffraction peaks and uncertain inputs of small strain and SFP were used. The turning points indicate that the gathered SFs become significant enough and the SFE calculation tends to be stabilized and reliable. The value calculated here at room temperature is slightly higher than that in [12] because of the different methods used to calculate $\langle\varepsilon_{50}^2\rangle_{111}$. It is noted that Mo addition to this HEA might reduce the SFE significantly as demonstrated in Fe-Cr-Ni system [32]. The dropping of SFE leads to the shifting of deformation mechanisms: deformation-induced twinning at 293 K with SFE of 28 mJm^{-2} [22], and at 77 K with SFE of 17 mJm^{-2}; whereas phase transformation (from γ-phase to ε-/α'- phase) occurred at 15 K with SFE of 11 mJm^{-2}.

Steinmetz's equation was used to calculate critical stress for twinning (σ_{tw}) [33]:

$$\sigma_{tw} = M\boldsymbol{\tau}_{\mathbf{tw}} = M\left(\frac{\gamma_{sf}}{3\boldsymbol{b}_p} + \frac{3G\boldsymbol{b}_p}{L_0}\right) \quad (4)$$

, where *G* is the shear modulus (85 GPa), $\boldsymbol{\tau}_{\mathbf{tw}}$ is the critical shear stress for twinning, $\boldsymbol{b}_p$ is the Burgers vector for partial dislocations (a_0<112>/6), *M* is the Taylor factor (3.06), and the L_0 is the width of the twin embryo (~200 nm) [12]. The calculated σ_{tw} decreases progressively from 767 MPa at 293 K to 642 MPa at 15 K. Experimentally, we used the stress at SFP = 0 (shown with red circles at Fig. 3b and 3d) as the critical stress for twinning, which are 710±30 MPa/2.5% true strain at 77 K and 670±30 MPa/0.45% true strain at 15 K

(Table 1). The values obtained by the two methods agree reasonably well. Although deformation-induced twinning and phase transformation are two exclusive strengthening mechanisms [34], the formation of twinning at low strain conditions may serve as nucleation sites for FCC-BCC/BCT phase transformation [35-37]. Hence the calculation of twinning stress at 15 K is relevant although the alloy tends to prompt phase transformation due to the reduced SFE at 15 K.

Table. 1 Properties of the $FeCoCrNiMo_{0.2}$ alloy at three temperatures

Temperature (K)	YS (MPa)	UTS (MPa)	Elongation (%)	Lattice Parameter (Å)	SFE_{-2} (mJm^{-2})	Measured (MPa)		Calculated (MPa)	
						τ_{tw}	σ_{tw}	τ_{tw}	σ_{tw}
293	376	767	52.5	3.5952	28	245±10	750±30	251	767
77	637	1212	71.2	3.5865	17	232±10	710±30	225	689
15	710	1423	41.8	3.5847	11	219±10	670±30	210	642

The phase transformation process during tensile test at 15 K was depicted at Fig. 4b, where the weight fraction of the three phases (γ, ε and α') obtained by Rietveld refinement in TOPAS [24] was plotted with respect to true stress, along with the SHR curve. During stage I (from 700 to 802 MPa), the SHR kept dropping whereas the phase fraction only changed slightly. The drop of SHR was due to dynamic recovery [38] and glide of partial dislocations in γ phase, serving as an incubation for the following phase transformation [39]. During stage II (from 802 MPa to 1270 MPa), the phase transformation occurred. At first, the phases transformed at an ultrafast speed within ~70 MPa, with α'-phase fraction soaring to ~42%, ε-phase to ~6% while γ-phase decreasing dramatically to ~52%. This mainly results from that the phase transformation originally occurred at favorable sites (i.e. grain boundaries and grains with preferred orientation). The phase transformation from FCC to BCC can trigger TRIP effect, which can enhance the strain hardening over a wide deformation range and improve the ductility significantly [40]. The induced massive γ-/α'-/ε- phase interfaces, can also serve as barriers against the (partial-) dislocation motion and strengthen the alloy [41, 42]. During the rest part of Stage II (from 870 to 1270 MPa), the phase transformation continued (α'-phase increased to ~81%, γ-phase decreased to ~16% and ε-phase disappeared gradually), however, with lower speed. This originates from that the phase transformation shifted to grain interior or not-so-good-orientated grains [15]. It also led to the slow-down of SHR growth. At stage III (>1270 MPa), the phase transformation reached a plateau (~87% for α'-phase and ~13% for γ-phase). Consequently, the SHR started to decrease since the supply of new phases was stopped.

In situ neutron diffraction measurements and tensile tests were applied to study the strengthening mechanisms of a high performance HEA alloy ($FeCoCrNiMo_{0.2}$) at 77 and 15 K. The alloy prepared composes of a single FCC phase, which exhibited astonishing mechanical properties at both temperatures (YS of 637 MPa, UTS of 1212 MPa and elongation of 71.2% at 77 K, while YS of 710 MPa, UTS of 1423 MPa and elongation of 42% at 15 K). The strength and ductility enhancement at 77 K mainly benefit from the interaction between twinning boundaries and dislocations, while phase transformation plays a majority role in strengthening at 15 K. The transition of strengthening mechanism can be ascribed to the temperature dependent SFE dropping, which was calculated to be 28, 17 and 11 mJ/m^2 at 298, 77 and 15 K, respectively. Hence, engineering SFE by tuning alloy composition and deformation temperature can induce desirable strengthening mechanisms (twinning and phase transformation), effectively improving the mechanical performance of alloys, which is a promising concept to exploit more advanced cryogenic HEAs.

The authors thank ISIS neutron and muon source (the Rutherford Appleton Laboratory, UK) for providing the beamtime (RB1720261 and RB1810732) and staff at ENGIN-X beamline for support. Y.L. and B.L. thanks the funding from the National Science Fund of China for Distinguished Young Scientists (51625404). B.C. thanks the support from the Diamond-Birmingham Collaboration.

References

[1] K.Y. Tsai, M.H. Tsai, J.W. Yeh, Acta Materialia 61(13) (2013) 4887-4897.
[2] Z. Lu, H. Wang, M. Chen, I. Baker, J. Yeh, C.T. Liu, T. Nieh, Intermetallics 66 (2015) 67-76.
[3] J.W. Yeh, S.-K. Chen, S.-J. Lin, J.-Y. Gan, T.-S. Chin, T.-T. Shun, C.-H. Tsau, S.-Y. Chang, Advanced Engineering Materials 6(5) (2004) 299-303.
[4] B. Cantor, I.T.H. Chang, P. Knight, A.J.B. Vincent, Materials Science and Engineering: A 375-377 (2004) 213-218.
[5] K. Liu, M. Komarasamy, B. Gwalani, S. Shukla, R.S. Mishra, Scripta Materialia 158 (2019) 116-120.
[6] Z. Tang, T. Yuan, C.-W. Tsai, J.-W. Yeh, C.D. Lundin, P.K. Liaw, Acta Materialia 99 (2015) 247-258.
[7] M. Bönisch, Y. Wu, H. Sehitoglu, Acta Materialia 153 (2018) 391-403.
[8] D. Wei, X. Li, W. Heng, Y. Koizumi, F. He, W.-M. Choi, B.-J. Lee, H.S. Kim, H. Kato, A. Chiba, Materials Research Letters 7(2) (2019) 82-88.
[9] B. Gwalani, S. Gorsse, D. Choudhuri, Y. Zheng, R.S. Mishra, R. Banerjee, Scripta Materialia 162 (2019) 18-23.
[10] Q. Lin, J. Liu, X. An, H. Wang, Y. Zhang, X. Liao, Materials Research Letters 6(4) (2018) 236-243.
[11] B. Gludovatz, A. Hohenwarter, D. Catoor, E.H. Chang, E.P. George, R.O. Ritchie, Science 345(6201) (2014) 1153-1158.
[12] Y. Wang, B. Liu, K. Yan, M. Wang, S. Kabra, Y.-L. Chiu, D. Dye, P.D. Lee, Y. Liu, B. Cai, Acta Materialia 154 (2018) 79-89.
[13] Z. Li, K.G. Pradeep, Y. Deng, D. Raabe, C.C. Tasan, Nature 534(7606) (2016) 227.
[14] S. Curtze, V.-T. Kuokkala, Acta materialia 58(15) (2010) 5129-5141.
[15] J.W. Bae, J.B. Seol, J. Moon, S.S. Sohn, M.J. Jang, H.Y. Um, B.-J. Lee, H.S. Kim, Acta Materialia 161 (2018) 388-399.
[16] S. Huang, H. Huang, W. Li, D. Kim, S. Lu, X. Li, E. Holmstrom, S.K. Kwon, L. Vitos, Nat Commun 9(1) (2018) 2381.
[17] J. Lu, L. Hultman, E. Holmström, K.H. Antonsson, M. Grehk, W. Li, L. Vitos, A. Golpayegani, Acta Materialia 111 (2016) 39-46.
[18] S. Liu, Y. Wu, H. Wang, J. He, J. Liu, C. Chen, X. Liu, H. Wang, Z. Lu, Intermetallics 93 (2018) 269-273.
[19] A. Zaddach, C. Niu, C. Koch, D. Irving, Jom 65(12) (2013) 1780-1789.
[20] F. Tian, L.K. Varga, N. Chen, L. Delczeg, L. Vitos, Physical Review B 87(7) (2013) 075144.
[21] Z.F. He, N. Jia, D. Ma, H.L. Yan, Z.M. Li, D. Raabe, Materials Science and Engineering: A 759 (2019) 437-447.
[22] B. Cai, B. Liu, S. Kabra, Y. Wang, K. Yan, P.D. Lee, Y. Liu, Acta Materialia 127 (2017) 471-480.
[23] O. Kirichek, J. Timms, J. Kelleher, R. Down, C. Offer, S. Kabra, S. Zhang, Review of Scientific Instruments 88(2) (2017) 025103.
[24] K. Yan, K.D. Liss, I.B. Timokhina, E.V. Pereloma, Materials Science and Engineering A 662 (2016) 185-197.
[25] X.S. Yang, S. Sun, H.H. Ruan, S.Q. Shi, T.Y. Zhang, Acta Materialia 136 (2017) 347-354.
[26] F. Sánchez-Bajo, F. Cumbrera, Journal of Applied Crystallography 30(4) (1997) 427-430.
[27] S. Kibey, J.B. Liu, D.D. Johnson, H. Sehitoglu, Acta Materialia 55(20) (2007) 6843-6851.
[28] J. Jeong, W. Woo, K. Oh, S. Kwon, Y. Koo, Acta Materialia 60(5) (2012) 2290-2299.
[29] B.E. Warren, X-ray Diffraction, Courier Corporation1990.
[30] R. Reed, R. Schramm, Journal of Applied Physics 45(11) (1974) 4705-4711.
[31] D. Balzar, H. Ledbetter, Journal of Applied Crystallography 26(1) (1993) 97-103.
[32] D. Molnár, G. Engberg, W. Li, S. Lu, P. Hedström, S.K. Kwon, L. Vitos, Acta Materialia 173 (2019) 34-43.
[33] D.R. Steinmetz, T. Jäpel, B. Wietbrock, P. Eisenlohr, I. Gutierrez-Urrutia, A. Saeed–Akbari, T. Hickel, F. Roters, D. Raabe, Acta Materialia 61(2) (2013) 494-510.
[34] M. Jo, Y.M. Koo, B.J. Lee, B. Johansson, L. Vitos, S.K. Kwon, Proc Natl Acad Sci U S A 111(18) (2014) 6560-5.
[35] T.S. Byun, N. Hashimoto, K. Farrell, Acta Materialia 52(13) (2004) 3889-3899.
[36] S.S. Sohn, S. Hong, J. Lee, B.-C. Suh, S.-K. Kim, B.-J. Lee, N.J. Kim, S. Lee, Acta Materialia 100 (2015) 39-52.

[37] Y.H. Jo, W.M. Choi, D.G. Kim, A. Zargaran, S.S. Sohn, H.S. Kim, B.J. Lee, N.J. Kim, S. Lee, Scientific Reports 9(1) (2019) 2948.
[38] A. Rohatgi, K.S. Vecchio, G.T. Gray, Metallurgical and Materials Transactions A 32(1) (2001) 135-145.
[39] A.K. De, J.G. Speer, D.K. Matlock, D.C. Murdock, M.C. Mataya, R.J. Comstock, Metallurgical and materials transactions A 37(6) (2006) 1875-1886.
[40] C. Herrera, D. Ponge, D. Raabe, Acta Materialia 59(11) (2011) 4653-4664.
[41] S. Martin, C. Ullrich, D. Rafaja, Materials Today: Proceedings 2 (2015) S643-S646.
[42] X. Gao, Y. Lu, B. Zhang, N. Liang, G. Wu, G. Sha, J. Liu, Y. Zhao, Acta Materialia 141 (2017) 59-66.

List of Figures

List of Tables

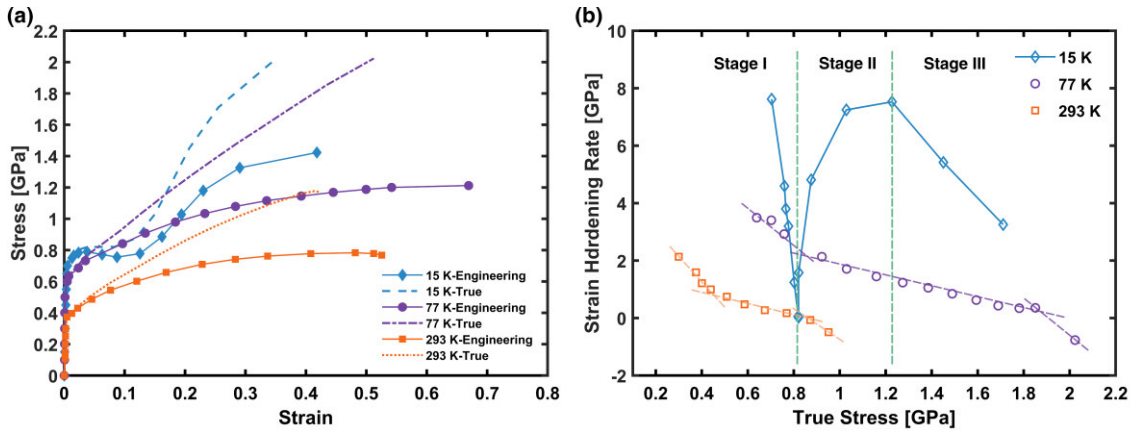

Fig. 1 (a) True strain-stress curve and (b) strain hardening rate curve at 293, 77 and 15 K.

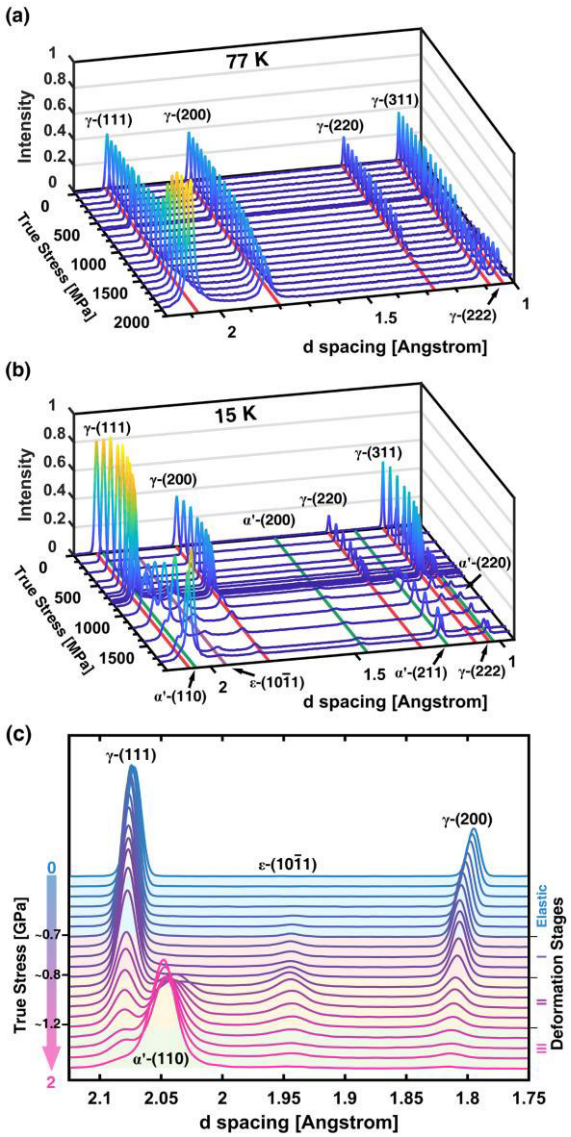

Fig. 2 Diffraction patterns during deformation at (a) 77 K, (b) 15 K and (c) 15 K, with higher magnification.

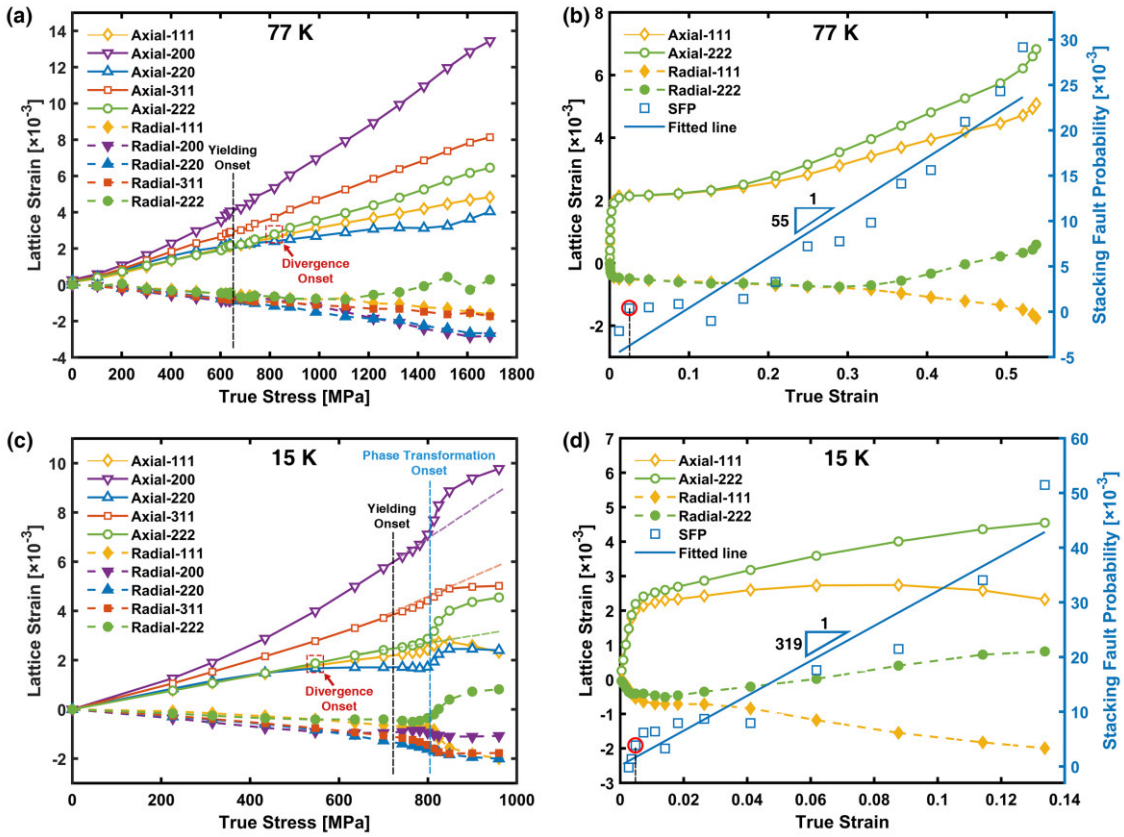

Fig. 3 Evolution of elastic lattice strain (a and c) and corresponding stacking fault probability (b and d) along axial and radial directions in crystallographic planes of (222), (311), (220), (200) and (111) during tensile tests at (a)(b) 77 K, (c)(d) 15 K. "Divergence onset" indicates the start point of the observable separation of the two lattice strain curves belonging to (111) and (222) grain plane.

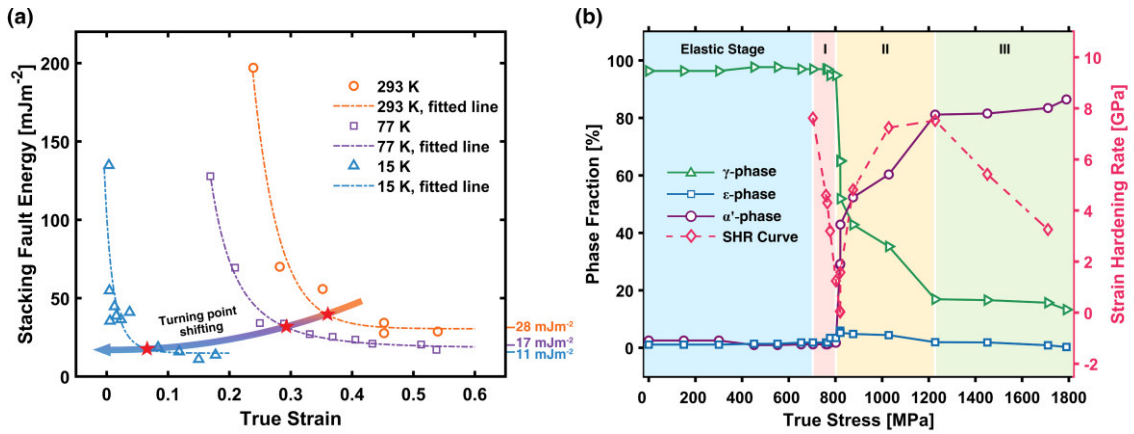

Fig. 4 (a) Stacking fault energy calculation curve at 293, 77 and 15 K and (b) fraction evolution of γ-, α'- and ε- phase and strain hardening rate curve as a function of true stress during deformation at 15 K.